



Installing earth-abundant metal active centers to covalent organic frameworks for efficient heterogeneous photocatalytic CO₂ reduction

Meng Lu^{a,1}, Qiang Li^{b,1}, Jiang Liu^{a,*}, Feng-Ming Zhang^c, Lei Zhang^a, Jin-Lan Wang^b, Zhen-Hui Kang^{d,*}, Ya-Qian Lan^{a,*}

^a Jiangsu Collaborative Innovation Centre of Biomedical Functional Materials, Jiangsu Key Laboratory of New Power Batteries, School of Chemistry and Materials Science, Nanjing Normal University, Nanjing, 210023, China

^b School of Physics, Southeast University, Nanjing, 211189, China

^c College of Chemical and Environmental Engineering, Harbin University of Science and Technology, Harbin, 150040, China

^d Jiangsu Key Laboratory for Carbon-based Functional Materials and Devices, Institute of Functional Nano and Soft Materials, Soochow University, Suzhou, 215123, China

ARTICLE INFO

Keywords:

Covalent organic frameworks
Transition-Metal
Carbon dioxide reduction
Heterogeneous catalyst

ABSTRACT

Photocatalytic conversion of CO₂ into energy carriers has been recognized as a highly promising strategy for achieving the virtuous carbon cycle in nature. The realization of this process depends on an efficient catalyst to reduce the reaction barrier. Herein, we report a series of transition metal ion modified crystalline covalent organic frameworks (COFs) for the heterogeneous photocatalytic reduction of CO₂. By coordinating different kinds of open metal active species into COFs, the resultant DQTP (2,6-diaminoanthraquinone - 2,4,6-triformylphloroglucinol) COF-M (M = Co/Ni/Zn) exerts a strong influence on the activity and selectivity of products (CO or HCOOH). Significantly, DQTP COF-Co exhibits a high CO production rate of $1.02 \times 10^3 \mu\text{mol h}^{-1} \text{g}^{-1}$, while DQTP COF-Zn has a high selectivity (90% over CO) for formic acid generation ($152.5 \mu\text{mol h}^{-1} \text{g}^{-1}$). This work highlights the great potential of using stable COFs as platforms to anchor earth-abundant metal active sites for heterogeneous CO₂ reduction.

1. Introduction

The continuous fossil fuel consumption has led to massive emission of greenhouse gases (mainly CO₂), causing severe environmental issues such as global warming and sea level rising [1–4]. Development of an approach for high-efficient conversion of CO₂ to high value-added substances with the assistance of renewable energy sources is highly important for the sustainable development of human society [5]. Artificial photosynthesis has currently emerged as one of the most promising ways to address the above issues. Using inexhaustible sunlight as driving force to reduce CO₂ to chemical fuels (CO, HCOOH, HCHO, CH₃OH, CH₄, etc.) is one of the most attractive ways [6–13]. Significantly, the exploration of suitable photocatalysts is critical for the effective execution of this catalytic process [14,15]. Generally, a suitable CO₂ reduction photocatalyst should possess a stable chemical construction, a strong light-harvesting ability, an efficient electron transport and CO₂ adsorption and activation ability [16,17]. Although many homogeneous molecular catalysts have been used for the photocatalytic CO₂ reduction with relatively high activity, their soluble

nature makes them difficult to be separated from the reaction mixture [18,19]. Additionally, their poor photocatalytic durability disallows the feasibility for practical utilization [20].

Considering these shortcomings, the construction of a heterogeneous photocatalyst is thus a more reasonable choice. Among the reported heterogeneous photocatalysts, metal-organic frameworks (MOFs) exhibit outstanding advantages in the photocatalytic reduction of CO₂, because they not only have the ability to absorb CO₂ molecules through their specifically functionalized channels but also can activate CO₂ molecule through their open metal sites [21–23]. However, the instability of their scaffolds linked by weak coordination bonds, as well as their inferior electronic conductivity make them less than satisfactory as photocatalysts. Therefore, their development in photocatalytic CO₂ reduction is severely limited. Consequently, increasing the bond strength and structural rigidity of porous materials while preserving the open metal active sites may be an appropriate strategy for realizing superior photocatalytic abilities.

Covalent organic frameworks (COFs) are a class of crystalline porous polymers that consist of strong covalent bonds and conjugated

* Corresponding authors.

E-mail addresses: liuj@njnu.edu.cn (J. Liu), zhkang@suda.edu.cn (Z.-H. Kang), yqlan@njnu.edu.cn (Y.-Q. Lan).

¹ These authors contributed equally.

layers with periodic skeletons and abundant regular pores [24]. In particular, two-dimensional COFs (2D-COFs) always display favourable structural robustness and efficient electron mobility, resulting in their extensive application in a variety of fields such as catalysis, gas storage, and electronics [25–29]. CO₂ adsorption and activation, electron transfer and structural stability can be achieved simultaneously by using rationally designed COFs. These characteristics of COFs appear to be more beneficial for the heterogeneous photocatalytic CO₂ reduction [30]. Additionally, a certain range of visible light adsorption is obtainable by adjusting the conjugated system and chromophore of COFs. A series of COFs and COF-based composites have recently been developed for photocatalytic water splitting [31–39], while researches on photocatalytic CO₂ reduction through COFs are still in the infancy [40–44]. However, in contrast to MOFs, COFs exhibit the prominent drawback of the lack of bare active metal centers that are crucial for activating the CO₂ molecule during the photocatalytic reaction. In this case, the development of active metal-modified COFs as photocatalysts is thus a more logical avenue towards improving the performance of heterogeneous photocatalytic CO₂ reduction.

With these considerations in mind, we focused on a 2D anthraquinone-contained COF, which possesses conjugated and rigid anthraquinone plane and porosity that are conducive to electron transport and CO₂ adsorption [45]. Most importantly, the anthraquinone group has proven to have strong metal bonding ability [46–49]. Besides, the suitable distance (3.621 Å) between the quinone oxygen atoms in the adjacent layers creates a feasible coordination environment for anchoring transition metal ions (TMI). We found that not only the loaded metal ions can serve as active sites in the photocatalytic CO₂ reduction, but also the types of TMI can modulate the reduced products. Herein, a series of TMI-modified DQTP COFs (DQTP COF-M, M = Co, Ni, Zn) were synthesized and used as heterogeneous catalysts in the photocatalytic CO₂ reduction reaction. To illustrate the crucial role of the quinone oxygen atom for immobilizing the metal ions in DQTP COFs, we also studied DATP COF (2,6-diaminoanthracene - 2,4,6-triformylphloroglucinol COF) with a similar COF structure. We replaced 2,6-diaminoanthraquinone with 2,6-diaminoanthracene to form DATP COF, which resulted in the lack of suitable oxygen coordination sites inside the COFs and showed only a weak bonding ability for anchoring the metal ions. As expected, DQTP COF-M demonstrated poor performance for CO₂ reduction.

It was found that the highest CO production rate of $1.02 \times 10^3 \mu\text{mol h}^{-1} \text{g}^{-1}$ (TON = 2.18 and TOF = 0.55 h^{-1}) was obtained by DQTP COF-Co, while DQTP COF-Zn showed a high selectivity for (90% over CO) formic acid generation ($152.5 \mu\text{mol h}^{-1} \text{g}^{-1}$, TON = 0.33 and TOF = 0.08 h^{-1}). To the best of our knowledge, this is the first report on metalized COFs as catalysts for the heterogeneous photocatalytic CO₂ reduction.

2. Material and methods

2.1. Chemicals

Cobalt acetate tetrahydrate ($\text{Co}(\text{OAc})_2 \cdot 4\text{H}_2\text{O}$, AR), zinc acetate dihydrate ($\text{Zn}(\text{OAc})_2 \cdot 2\text{H}_2\text{O}$, AR), nickel acetate tetrahydrate ($\text{Ni}(\text{OAc})_2 \cdot 4\text{H}_2\text{O}$, AR), *N,N*-dimethylacetamide (DMA, AR), *N,N*-dimethylformamide (DMF, AR), tetrahydrofuran (THF, 99.5%), 1,3,5-trimethylbenzene (AR, $\geq 99.5\%$), acetic acid (AR, $\geq 99.8\%$) were purchased from Sinopharm Chemical Reagent Co., Ltd. 2,6-diaminoanthraquinone (DQ, $\geq 97\%$) was bought from Aladdin Industrial Corporation. 2,6-diaminoanthracene (DA, $\geq 95\%$) was bought from Jilin Province Extension Technology Co., Ltd. 2,4,6-triformylphloroglucinol (TP, $\geq 95\%$) was bought from Shanghai Kaiyulin Pharmaceutical Technology Co., Ltd.

2.2. Synthesis of DQTP COF

The synthesis of DQTP COF was carried out using a previously reported protocol with slight modification [45]. A schlenk tube measuring $19 \times 65 \text{ mm}$ (o.d \times length) was charged with DQ (34 mg, 0.15 mmol), TP (20 mg, 0.1 mmol), *N,N*-dimethylacetamide (0.8 mL), 1,3,5-trimethylbenzene (0.4 mL), and 6 M aqueous acetic acid (0.1 mL). After sonication for about 20 min, the tube was flash frozen at 77 K (liquid N₂ bath). Hereafter three freeze-pump-thaw cycles were conducted, then evacuated it to vacuum and sealed. After the mixture was allowed to warm to room temperature, it was heated at 120 °C and left undisturbed for 72 h. A dark red precipitate was isolated by filtration in Buchner funnel, followed by washing with DMA or DMF until the filtrate turned to colorless. After that, the wet sample was transferred to a Soxhlet extractor and washed with THF (24 h) and acetone (24 h). Finally, the product was evacuated at 150 °C under dynamic vacuum overnight to yield activated sample.

2.3. Synthesis of DATP COF

The synthesis of DATP COF was carried out using a previously reported protocol with modification [50]. A schlenk tube measuring $19 \times 65 \text{ mm}$ (o.d \times length) was charged with 2,6-diaminoanthracene (DA; 31.2 mg, 0.15 mmol) and 1, 3, 5-triformylphloroglucinol (TP; 20 mg, 0.1 mmol) in Dioxane (1 mL) with catalytic amount of 6 M acetic acid (0.2 mL). The reaction mixture was then sonicated for 20 min. After that, the tube was flash frozen at 77 K (liquid N₂ bath). Hereafter three freeze-pump-thaw cycles the system then evacuated to vacuum and sealed. After the mixture was allowed to warm to room temperature, it was heated at 120 °C and left undisturbed for 72 h. A brownish red precipitate was collected by filtration and subsequently washed by THF, water and acetone. Finally, the compound was dried at 150 °C by degassing to obtain a dark reddish-brown powder as activated DATP-COF.

2.4. Loading of Co(II) into DQTP COF / DATP COF

DQTP COF-Co(II) / DATP COF-Co(II) were synthesized by direct metallation of DQTP COF (DATP COF) with $\text{Co}(\text{OAc})_2 \cdot 4\text{H}_2\text{O}$ in a hydrothermal reaction. The experimental method of COF-Co(II) is given below as an example. DQTP COF (DATP COF) (100 mg) and Co ($\text{OAc})_2 \cdot 4\text{H}_2\text{O}$ (2.49 g, 0.01 mol) were added to the H₂O (100 mL). After sonication for about 20 min to ensure the thorough dissolution of cobalt acetate, the mixture was heated and refluxed for 72 h. Following that, the solutions were cooled down to room temperature and filtered. The filter cake was washed thoroughly with water and ethanol to remove free metal ions. The final filter cake was dried at 100 °C under dynamic vacuum overnight to get DQTP COF-Co(II) / DATP COF-Co(II).

2.5. Loading of Ni(II)/Zn(II) into DQTP COF / DATP COF

DQTP COF-Ni(II)/Zn(II) and DATP COF-Ni(II)/Zn(II) were synthesized following the synthetic procedures used for DQTP COF-Co(II) except that $\text{Co}(\text{OAc})_2 \cdot 4\text{H}_2\text{O}$ (2.49 g, 0.01 mol) was replaced by Ni ($\text{OAc})_2 \cdot 4\text{H}_2\text{O}$ (2.488 g, 0.01 mol) / $\text{Zn}(\text{OAc})_2 \cdot 2\text{H}_2\text{O}$ (2.19 g, 0.01 mol).

2.6. Material characterization

The powder X-ray diffraction (PXRD) spectra were recorded on a Bruker D8 Advance diffractometer at 40 kV, 40 mA with Cu-K α ($\lambda = 1.5418 \text{ \AA}$). X-ray photoelectron spectroscopy (XPS) test was conducted in an Escalab 250Xi instrument from Thermo Scientific equipped with an Al K α microfocused X-ray source, and the C1s peak at 284.6 eV was used as internal standard. The UV-vis absorption spectra were recorded on a Shimadzu UV-2450 spectrophotometer. Fourier Transform Infrared spectrum using the KBr pellet was measured on a

Bruker Tensor 27 in the range of 4000–400 cm^{-1} . Thermogravimetric analysis (TGA) was carried out on a Netzsch STA449F3 analyzer at a heating rate of 10° C/min from ambient temperature to 800° C. Elemental analysis (EA) was conducted using an Elementar vario EL III analyzer. Inductively Coupled Plasma (ICP) analysis was measured using Inductively Coupled Plasma Atomic Emission Spectrometer (Prodigy, The U.S.A). Nitrogen adsorption–desorption isotherms were measured at 77 K on an Autosorb IQ2 absorptiometer (Quantachrome Instruments), and CO_2 adsorption isotherms were measured at 298 K. Before the measurement, the sample was first degassed at 120° C for 12 h.

2.7. Photocatalytic measurement

The photocatalytic CO_2 reduction reaction (CO_2RR) activities of all the catalysts were carried out in a sealed quartz reactor at a constant temperature by using a thermostatic water bath. We apply the as-synthesized DQTP COF / DATP COF based catalysts for visible light-driven photocatalytic CO_2 reduction in a solvent of acetonitrile (MeCN) under mild reaction conditions (20° C and 1 atm. of CO_2), with triethanolamine (TEOA) as sacrificial reducing agent and $\text{Ru}(\text{bpy})_3\text{Cl}_2 \cdot 6\text{H}_2\text{O}$ as photosensitizer. The detailed procedure is as follows: 20 mg of the sample was uniformly dispersed in a solvent mixture of 50 ml (MeCN/TEOA = 4:1, v/v) through sonication for about five minutes, then 22.5 mg of $\text{Ru}(\text{bpy})_3\text{Cl}_2 \cdot 6\text{H}_2\text{O}$ was added, sonicated and stirred until dissolved. After bubbled by high-purity CO_2 for 30 min to remove air, the reactor was sealed. A 300 W xenon arc lamp with a cut filter (≥ 420 nm) was used as the light source. The mixture was kept stirring during the photocatalytic reaction. The gas products were measured using gas chromatography (GC-7920A, Aulight Co., China) with an FID detector to quantitative CO/ CO_2 and a TCD detector to quantitative H_2 . The liquid products were measured using ion chromatography (LC-2010 PLUS, Shimadzu, Japan). The isotope of ^{13}C was analyzed using gas chromatography-mass spectrometry (JEOL-GCQMS, JMS-K9 and 6890 N Network GC system, Agilent Technologies).

3. Results and discussion

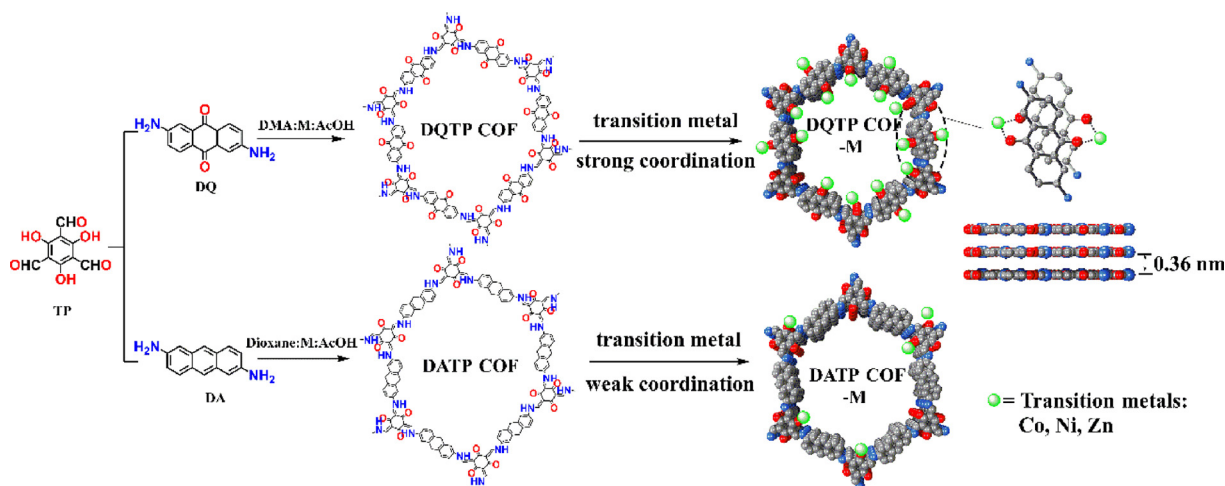
3.1. Structural and morphological characterization

DQTP COF and DATP COF were respectively prepared by the condensation of 2,6-diaminoanthraquinone (DQ) and 2,6-diaminoanthracene (DA) with 1,3,5-triformylphloroglucinol (TP) following Schiff-base reaction [51,52] using the previously reported procedures [45,50], as detailedly described in the above section. TMI-modified DQTP COF and DATP COF were synthesized by direct metallation of COF with

transition metal acetate via a simple hydrothermal method (Scheme 1, details also given in the Material and methods section).

The powder X-ray diffraction (PXRD) pattern of the as-synthesized DQTP COF matched the simulated pattern well, and the sharp diffraction peaks demonstrated high crystallinity of the sample. A series of characteristic signals at 3.5°, 5.9°, 7.0°, and a broad peak at 26.7° were in accordance with the $P6/m$ space group of DQTP COF that represented a hexagonal 2D layered network with an eclipsed AA stacking mode. After metallization, no additional peaks appeared and the only observable change was the slightly decreased intensity of the peaks, confirming the retention of the COF structure (Figs. 1a) [53,54]. We then studied the DATP COF as its structure is similar to DQTP COF except the lack of quinone oxygen group [55]. For comparison, the metallation procedure used for DATP COF was the same as that for DQTP COF and the corresponding structure was confirmed by the PXRD patterns (Fig. 1b) [50].

The porosity and surface areas of DQTP COF and DQTP COF-M were measured by nitrogen adsorption/desorption analysis at 77 K, showing type IV N_2 adsorption isotherms. The Brunauer–Emmett–Teller (BET) surface area decreased largely after metallization. Specifically, the BET surface area of host DQTP COF was $708.36 \text{ m}^2 \text{ g}^{-1}$, which decreased to 195.92, 172.15 and $345.57 \text{ m}^2 \text{ g}^{-1}$ after loading of Co, Ni and Zn, respectively (Figure S1a and Table S1). Besides, the pore size distribution of DQTP COF-M revealed significant reduction. Compared to the pore size distribution (10.2, 23.0 and 43.5 Å) before metal loading, DQTP COF-Co exhibited smaller pore sizes (10.2, 14.3 and 40.8 Å) after metal loading (Figure S1b and Table S2). These results confirmed the successful impregnation of TMIs into COF frameworks, as demonstrated in other similar works [54,56]. Additionally, X-ray photoelectron spectroscopy (XPS) measurement was conducted to further verify the successful loading of different TMIs into the pristine DQTP COF (Fig. 1c and S2). The observed Co $2p_{3/2}$ binding energy of 780.8 eV with a shakeup satellite at 786.2 eV in DQTP COF-Co was consistent with Co (II), while the Ni $2p_{3/2}$ binding energy at 855.6 eV (with a shakeup satellite at 861.5 eV) and Zn $2p_{3/2}$ binding energy at 1022.2 eV corresponded to Ni(II) and Zn(II), respectively (Figure S3). The characteristic binding energy shift of DQTP COF-M compared to that of the pure metal salt can prove the interaction between TMI and COFs. As for DQTP COF-Co, the Co $2p_{3/2}$ binding energy shifted from 784.3 eV (pure cobalt acetate) to 780.8 eV (Fig. 1d), because the carbonyl group in COFs tends to donate electrons to Co(II) ion and then makes the Co species less electron-deficient, as demonstrated in other TMI-modified matrix [54]. Moreover, the fine O1s XPS spectrum of DQTP COF-Co revealed the presence of Co–O bonds (Figure S4). These results stem mainly from the coordination interaction between Co(II) ion and the carbonyl group of the anthraquinone ligand on DQTP COF. We then conducted



Scheme 1. Synthesis and metallization of DQTP COF and DATP COF.

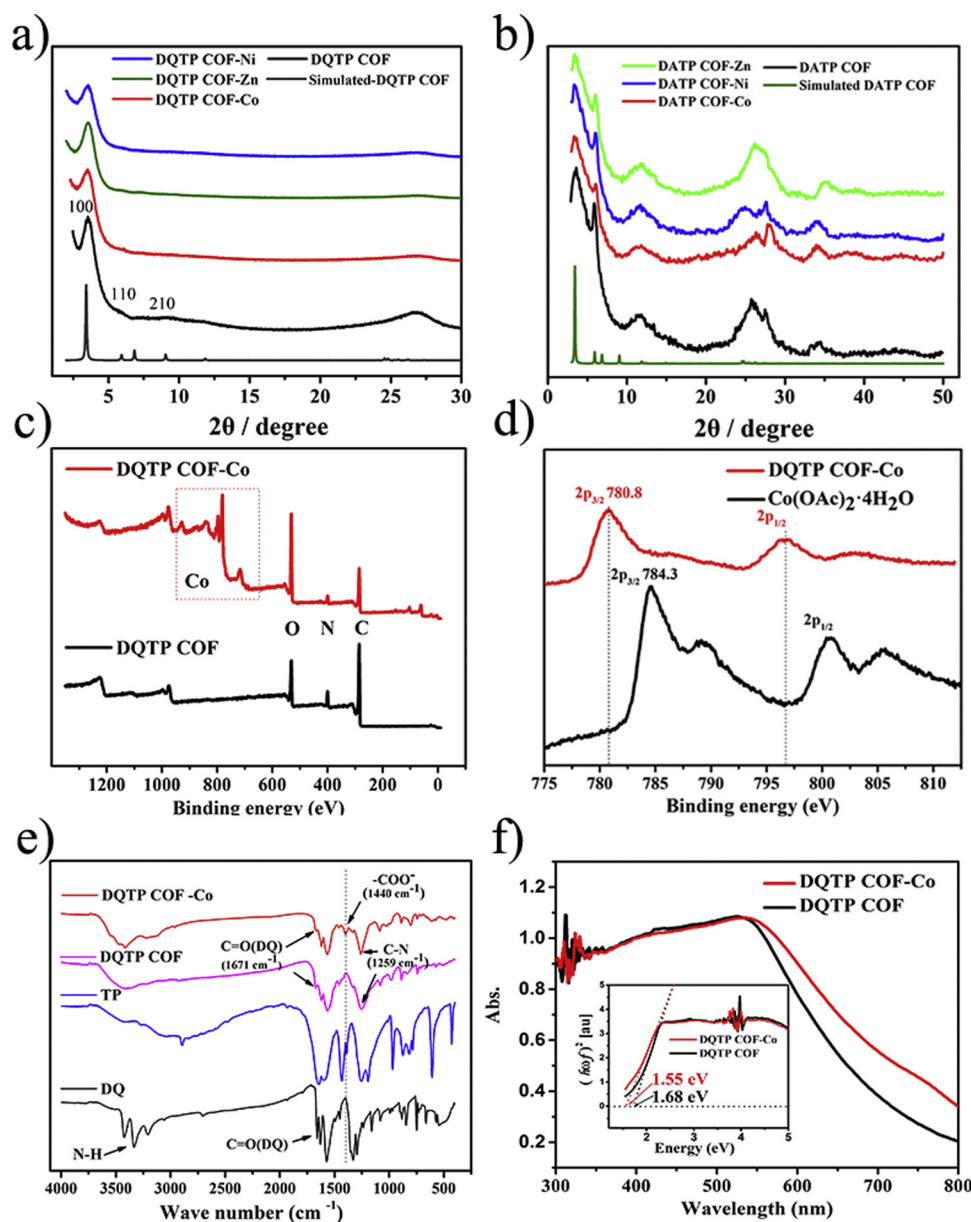


Fig. 1. Characterization of COFs. a) PXRD patterns of DQTP COF, DQTP COF-M and simulated DQTP COF; b) PXRD patterns of DATP COF, DATP COF-M and simulated DATP COF; c) Survey scan XPS profile of DQTP COF-Co (red) and DQTP COF (black); d) Comparative Co 2p XPS spectra of DQTP COF-Co and pure Co(OAc)₂·4H₂O; e) FTIR spectra of DQTP COF-Co. The absorption peak at 1440 cm⁻¹ can be assigned to the acetate groups; f) Solid-state UV-vis spectra of DQTP COF-Co (red) and pure DQTP COF (black), inset with Tauc plots and bandgap calculation (For interpretation of the references to colour in this figure legend, the reader is referred to the web version of this article).

FTIR spectroscopy, thermogravimetric analysis (TGA) (Figure S5) solid-state UV-vis spectroscopy, and local energy-dispersive X-ray (EDX) measurements to further investigate the incorporation of TMI into DQTP COF. For DQTP COF-Co, the absorption peak at 1440 cm⁻¹ in the FTIR spectra of DQTP COF-Co was assigned to the acetate group (C–O stretching band) of the incorporated Co(OAc)₂. An obvious blue shift compared to the pure cobalt acetate tetrahydrate (1417 cm⁻¹) was detected due to the p- π conjugation effect between the oxygen atom and the aromatic ring in COF (Fig. 1e) [57]. The UV-vis absorption spectra of DQTP COF-Co/Ni/Zn extended to a broader region compared to the host DQTP COF, which was related to the increased degree of delocalization due to the chelation of TMIs (Fig. 1f and Figure S6). At the same time, the electronic conductivity of DQTP COF-M was also found to be better than that of the host COF from electrochemical impedance spectroscopy (EIS) measurements, as indicated by the radius of the preceding semicircle (Figure S7), suggesting the introduction of transition metals into COFs can obviously enhance the charge transfer. Scanning electron microscopy (SEM) and transmission electron microscopy (TEM) were carried out to examine the morphology of DQTP COF-M materials. From Figs. 2a–b and S8–11, SEM (Figure S8,

magnification: 20,000X) and TEM (Figure S10, magnification: 50,000X) images show that the morphology of DQTP COF and DQTP COF-M were almost the same. To explore the morphology changes in detail, we further conducted a higher resolution SEM test (Figure S9, magnification: 50,000X) and TEM test (Figure S11, magnification: 80,000X). Apparently, both DQTP COF and DQTP COF-M showed multi-layer overlapping nano-sheets as seen on the edge, and no significant morphology changes were noted between the two. These results also confirmed the structural stability of the COFs platform. Besides, no nanoparticles were observed on the surface of the DQTP COF-M, and EDS mapping revealed the uniform distribution of the cobalt atoms (Fig. 2c–h and S12–14). Thus, all of the above analysis results again corroborated that Co(II), Ni(II) and Zn(II) TMIs were successfully anchored on DQTP COF. The amounts of TMI coordinated into DQTP COF were quantified by TGA, inductively coupled plasma (ICP) and EDX analysis, finally revealing a relatively average metal content of 6.7 (wt.%) in the host framework (Tables S3–S5).

FTIR spectroscopy and TGA measurements were also performed to investigate the TMI-loaded DATP COF. Barely no characteristics of metal coordination were detected from the FTIR spectrum (Figure S15),

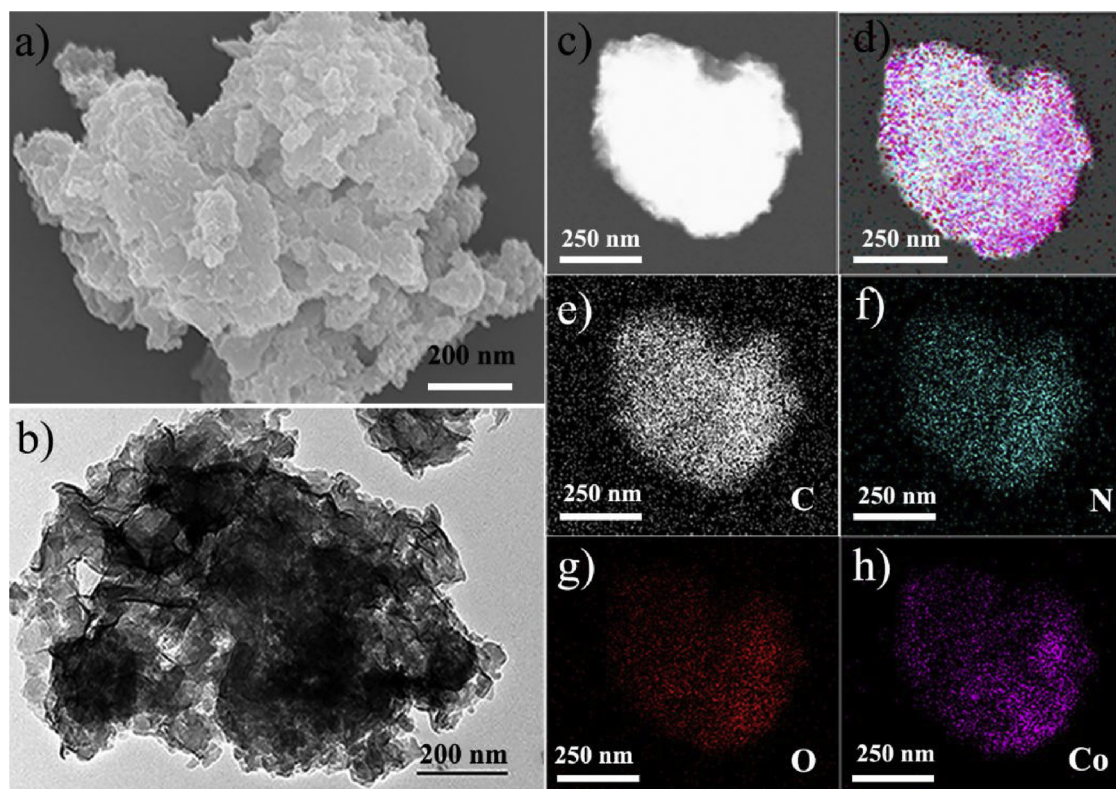


Fig. 2. The morphology and elements distribution of COFs. a) SEM image of DQTP COF-Co; b) TEM image of DQTP COF-Co; HRTEM mapping image of DQTP COF-Co: c) Dark field image; d) Mixed element map and mappings of e) C, f) N, g) O and h) Co.

and the TGA results showed a small residue amount after 800 °C in the oxygen atmosphere (Figure S16). There were only trace amounts of metal content remained due to surface adsorption in bulk COF materials and the difficulty to remove them through washing. These comparison test results confirmed that the metal ions are highly possible to be loaded in the quinone oxygen group of DQTP COF.

Density functional theory (DFT) calculation was applied to understand the coupling between transitional metals and DQTP COF, and Zn was chosen as an example. Since Zn can coordinate with the organic species of either O or N, we consider four possible binding sites as presented in Fig. 3a and hence to identify the active sites for further catalytic reactions. The coupling of Zn with two types of interlayer oxygen atoms is illustrated in Fig. 3b and c with Zn-O distance being 2.61 and 2.14 Å, which suggests the formation of coordination bonding. Furthermore, the O-Zn-O bonding promotes the interlayer interaction by shortening the interlayer distance to 3.4 and 3.3 Å, respectively. It was found from the comparison between the two couplings that the interaction between Zn with quinone oxygen atoms gives rise to a

stronger binding by 0.16 eV per Zn atom ($E_1 - E_2/N_{Zn}$). On the contrary, N-containing coordination of configuration 3 and 4 in Fig. 3a failed to stabilize the Zn atoms. As shown in Movie 1 and 2, the initial Zn-N distance is set to be ~ 2 Å, and both configurations turn back into the coordination with interlayer oxygens and Zn-N enlarges to more than 4 Å at the end of a simple optimization procedure. The calculations agreed well with the experimental result that the transitional metals were primarily anchored between the interlayer quinone oxygen atoms.

To examine the semiconductor character of these TMI-modified DQTP COFs and their suitability for subsequent use in photocatalytic conversion of CO₂, UV-vis diffuse reflectance spectroscopy (DRS) associated with Mott – Schottky measurements (MS) were conducted to determine the electronic properties of COFs (Figures S6 and S17–20). Since the bottom of the conduction band (LUMO) in n-type semiconductors is commonly close to the flat-band potential, LUMO locations of DQTP COF-M were estimated to be -0.53 V (DQTP COF, vs. NHE), -0.95 V (DQTP COF-Co, vs. NHE), -1.17 V (DQTP COF-Ni, vs. NHE) and -0.61 V (DQTP COF-Zn, vs. NHE), respectively. The

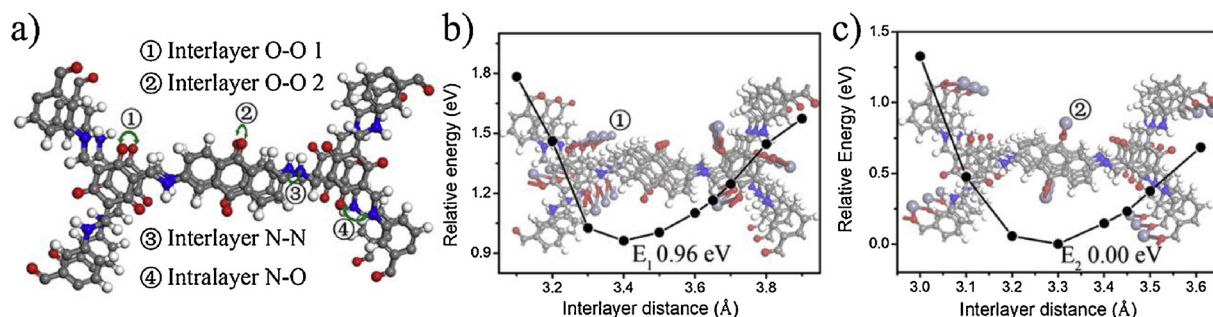


Fig. 3. DFT calculations results of DQTP – COF-M. a) Four possible coordination sites for metal atoms in the DQTP COF framework. b) and c) relative energies of transitional metal anchored on interlayer oxygens along with interlayer distance changing, and the lowest energy of configuration 2 at interlayer distance of 3.3 is set to 0.00 eV as E_2 .

negative conduction band edge shift of DQTP COF-Co, Ni and Zn compared to the metal-free COF corresponded to the delocalized intramolecular charge transfer (ICT) from COFs to coordinated metal complex. In view of such negative potentials for LUMO in TMI-modified DQTP COFs, theoretically, CO₂ molecules can be converted into many products such as CO and HCOOH upon visible-light irradiation [58] (Figures S21–23).

3.2. Photocatalytic performance

To evaluate the photocatalytic CO₂ reduction activity of the three as-synthesized TMI-modified COFs catalysts (DQTP COF-Co, Ni and Zn, respectively), acetonitrile (MeCN) was selected as reaction solvent because of its high solubility for CO₂ [59]. Photocatalytic reaction was conducted under pure CO₂ (1.0 atm, 293 K) atmosphere using triethanolamine (TEOA) and Ru(bpy)₃Cl₂·6H₂O (bpy = 2,2'-bipyridine) as the sacrificial agent and the photosensitizer, respectively (details are in the Experiment section). Based on the time-dependent conversion yields of CO₂ to CO for these three transition-metal modified COFs, DQTP COF-Co showed the highest activity of 81.49 μmol after 4 h reaction, which is 4.5–55 times higher than that of the other DQTP COF-M (DQTP COF-Ni, 18.35 μmol, TON = 0.5; DQTP COF-Zn, 1.45 μmol, TON = 0.04), as shown in Fig. 4a. These results suggested that the significant difference in the activity for photocatalytic CO₂ conversion was mainly induced by different TMIs bonded in COFs and the mechanism was discussed as follows.

By contrast, DATP COF-Co exhibited poor photocatalytic performance (8 times smaller CO yield compared to DQTP COF-Co) because of the lack of effective active metal sites inside the framework (Fig. 4b). The time-dependent conversion yields of CO and H₂ for DQTP COF-Co were tested, and a CO selectivity (59.4%) over H₂ was achieved and no other gas products were observed in the reaction system (Figures S24 and S25). To confirm the carbon source of CO, MS (mass spectrometry) of ¹³CO (*m/z* = 29) was performed by using ¹³CO₂ as the reactant atmosphere, confirming that the product CO is derived from gaseous CO₂ rather than from other sources such as catalyst or solvent decomposition (Fig. 4c). A series of control experiments including the use of different sacrificial electron donors and solvent composition were performed to investigate the corresponding effect of these factors on the photocatalytic CO₂ reduction by using DQTP COF-Co as an example. When the photocatalytic reaction were carried out in absence of electron donor (Table S6, entry 4), photosensitizer (Table S6, entry 7), light irradiation (Table S6, entry 8), and catalyst (Table S6, entry 10), and in the atmosphere of N₂ instead of CO₂ (Table S6, entry 6), there were no carbon-based products detected in the final gas phase and liquid phase in our system. These results implied that all of the aforementioned components are necessary for the execution of photocatalytic CO₂ reduction reaction. Firstly, three kinds of common sacrificial electron donors, TEOA (triethanolamine), TEA (triethylamine) and TIPA (triisopropanolamine), were independently used in the photocatalytic reaction (Entry 1, 2 and 3 in Table S6). We found that using TEOA as electron donors tends to generate gaseous product CO (41.47 μmol after 4-h test) while TEA and TIPA are more easily to yield liquid product HCOOH (34.87 μmol for TEA and 33.38 μmol for TIPA over a period of 4 h). To the best of our knowledge, study on the selection of sacrificial electron donors towards the photocatalytic product selectivity is still rarely reported, and the influence mechanism behind them is also complicated and needs to be further validated [60]. Secondly, we found that the solvent composition was another apparent influence factor on photocatalytic performance in our system. When the photocatalytic reaction was conducted under the condition of MeCN/TEOA = 4:1, gaseous CO generation can reach up to 41.47 μmol. But only a little amount of HCOOH (5.64 μmol) instead of CO was obtained in reaction solution of H₂O/TEOA = 4:1 (Table S6, entry 5). Moreover, the increased production rate of HCOOH (94.68 μmol), together with a trace amount of CO, can be observed by using DMA/TEOA (4:1) mixture

solution. It is obvious that high yield and activity of reductive products can be realized in MeCN or DMA reaction solvent, due to which primarily has better CO₂ solubility than H₂O. The polarity, dielectric constant and metal-bonding ability of different solvents are also having an effect on stabilizing specifically intermediate product and then the whole photocatalytic process [35]. Additionally, the photocatalytic experiments under different MeCN / TEOA ratios (24:1, 12:1, 4:1 and 2:1) were tested, and the pH of solutions maintained its own state without additional control because the pH values on different MeCN/TEOA ratios are approximate. The pH values before CO₂ saturated are 9.97–10.71, while they change to 9.15–8.72 after CO₂ saturated, slightly acidic. These values are too close to consider the effect of pH on the reaction. The test results are shown in Figure S26. We found that the CO evolution promoted distinctly as TEOA proportion increases and reaches a maximum in 4:1. The influence of TEOA concentration of reaction solution on the photocatalytic CO₂ reaction rate is also reported in previous literature [61]. Reasons accountable for our results include: 1) From the aspect of reaction mechanism: During the photocatalysis process, the photosensitizer is activated to an excited state under visible light irradiation, which is then quenched by TEOA serving as sacrificial electron donor. The efficient electron transfer from TEOA to photosensitizer/catalyst requires a suitable concentration environment through chemical kinetic theory. Besides, a high concentration of TEOA is always required to enhance CO₂ photoreduction reaction efficiency [62]. From the aspect of reaction kinetics: 2) TEOA also plays a role as a proton source in our photocatalytic reaction system and high TEOA concentration is conducive to successful proton transfer of the catalyst [63]. 3) In MeCN/TEOA solutions the dissolved carbon dioxide will react with solvated tertiary amine to form an ion pair as follows: R₃N (HSol) + CO₂ → R₃NH⁺CO₂Sol⁻, where HSol designates solvent, R = CH₃CH₂OH [64]. Therefore, the more concentrated the TEOA solvent is, the more amount the CO₂ molecules can be absorbed, which is beneficial to CO₂ reduction reaction. Last, the crystallinity influence of DQTP COF-Co material was studied. As expected, the poor crystallinity indeed resulted in a lower photocatalytic activity in our system. We thought that only a few TMIs could be captured into COFs in this case because of stacking faults of internal structure and lost porosity, and thus establishing very limited photocatalytic active sites. Another reason could be that the stacking faults and smaller extension of π-system in poorly crystallized COFs might block the path for charge carriers transferring to active centers, that is, low charge carrier mobility [31]. The influence of different quantity of the catalyst and photosensitizer (using DQTP COF-Co as an example) on the evolution of CO was also investigated; it was found that the CO yield was positively correlated with the increase in the catalyst quantity (Fig. 4d). Additionally, the efficiency of CO yield is almost in linear relation with the amount of photosensitizer (Figure S27), indicating that more excited photoelectrons from the photosensitizer to transfer towards catalyst can indeed improve the reaction efficiency kinetically. The photocatalytic stability of DQTP COF-M was evaluated using recycling tests. As observed from the time course plots of CO evolution, these TMI-modified COFs maintain excellent photocatalytic activity during five cycles (Fig. 4e), and the slight decay in the subsequent runs is possibly a result of the mass loss in the recovery process of the used samples. No significant changes were observed from the XPS and PXRD patterns before and after the photocatalytic reaction recycling tests. The XPS patterns showed that DQTP COF-Co still maintained the valence of cobalt after recycling tests (Figure S28). The PXRD patterns showed that DQTP COF-Co kept the structure and crystallinity of the material after recycling tests (Figure S29). These results confirmed the structural robustness and heterogeneous photocatalytic durability. After the photocatalytic experiment, the possible liquid reductive products in the reaction solution were analyzed by ion chromatography (Figure S30). As shown in Fig. 4f, formic acid was detected with the highest selectivity (90% over CO) by DQTP COF-Zn (152.5 μmol h⁻¹ g⁻¹, TON = 0.33 and TOF = 0.08 h⁻¹).

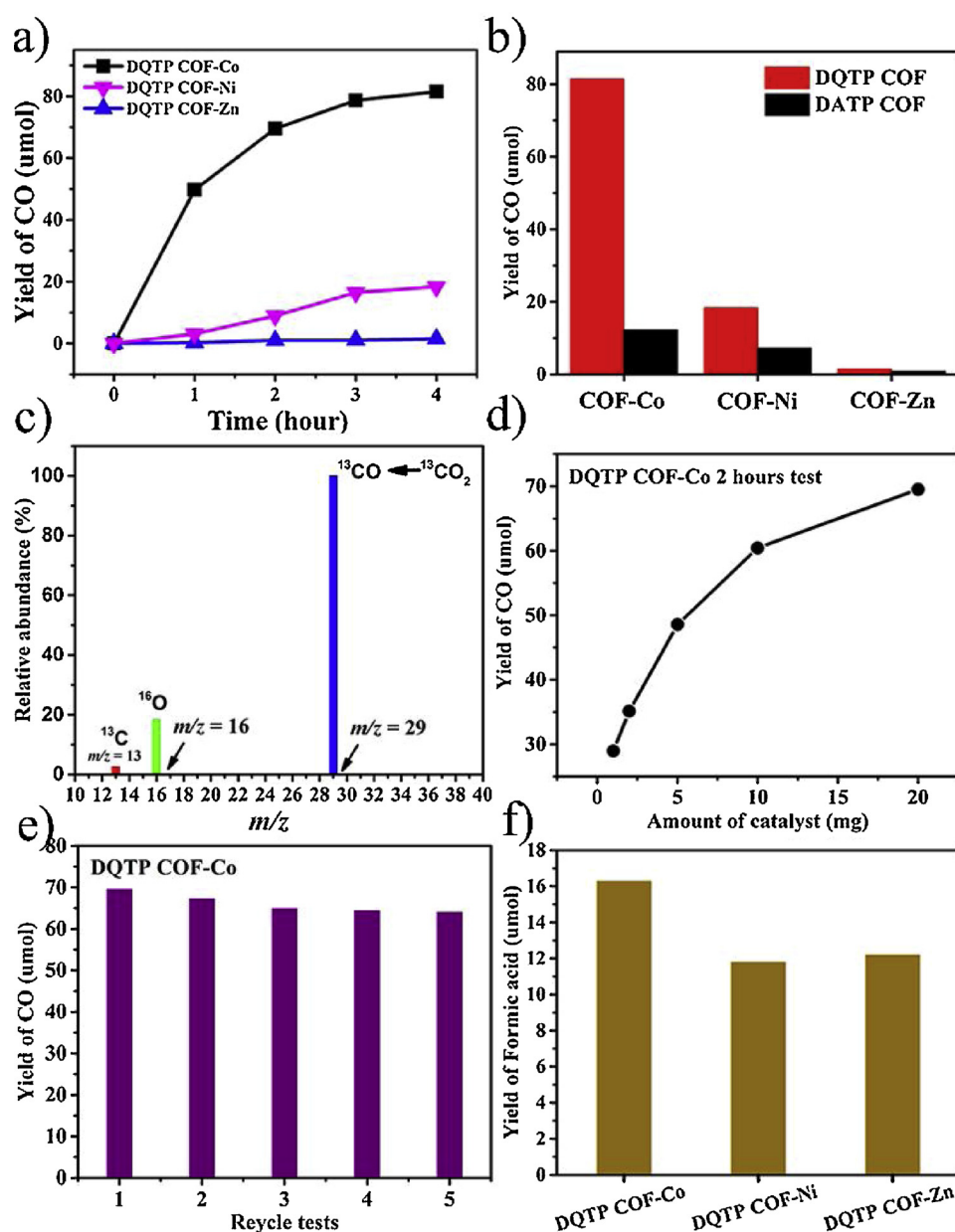


Fig. 4. Photocatalytic performance of COFs. a) Comparison of photocatalytic activity of DQTP COF-Co (black), Ni (pink) and Zn (blue) for CO evolution, respectively; b) Comparison of the conversion yields of CO for DQTP COF and DATP COF; c) MS of ^{13}CO ($m/z = 29$) produced from the photocatalytic reduction of $^{13}\text{CO}_2$ using DQTP COF-Co. d) CO production on different amounts of DQTP COF-Co; e) Recycling tests of DQTP COF-Co on evolution of CO by photocatalytic CO_2 reduction (2 h test); f) The liquid products evolved from DQTP COF-Co, Ni, Zn on photocatalytic reduction of CO_2 (For interpretation of the references to colour in this figure legend, the reader is referred to the web version of this article).

3.3. Mechanism for the photocatalytic CO_2 reduction reaction

Based on the photocatalytic results obtained here, a “two-pathway” mechanism for the photocatalytic CO_2 reduction reaction was proposed (Fig. 5). Photoluminescence (PL) and time-resolved fluorescence decay techniques were conducted to investigate the intramolecular charge transfer (ICT) behavior of COFs. The results showed that the PL intensity of DQTP COF-Co was significantly quenched compared to the host DQTP COF, and became weaker when introducing TEOA to the catalytic system (Fig S31). The average fluorescence life expectancy of DQTP COF-PS and DQTP COF-Co-PS are 8.28 and 8.16 ns (Fig S32–34), respectively, which decreased obviously with TEOA (3.97 ns) (Fig S33). It is suggested that the recombination of excited state was suppressed by incorporating Co active sites to COFs (electrons transfer occurs from COF to Co(II) after photoexcitation electron-hole separation), and the hole was scavenger by TEOA. Under the irradiation of visible light, $[\text{Ru}(\text{bpy})_3]^{2+}$ (PS) is converted to the excited state $^*[\text{Ru}(\text{bpy})_3]^{2+}$ (PS*). The photogenerated electrons were then transferred to COF due to the matched LOMO positions of DQTP COF-M and $[\text{Ru}(\text{bpy})_3]^{2+}$ [20]. The TEOA sacrificial electron donors consumed the produced holes in the

photosensitizer, while DQTP COF-M received photogenerated electrons and delivered them to the adsorbed CO_2 molecules in the transition metal. The adsorbed CO_2 tended to form a bent pattern and showed high reactivity as the LUMO level of CO_2 decreased to form $\text{CO}_2^{\cdot-}$ species [65]. Subsequently, the activated $\text{CO}_2^{\cdot-}$ intermediate can follow two alternative pathways to obtain the final reductive product (HCOOH or CO), mainly involving C–O bond cleavage or proton adduct (COOH^{\cdot}), as demonstrated in other works [66,67]. Based on our test results, these three different TMI-modified COFs showed obvious distinguishing photocatalytic efficiency and selectivity. Such a fact can be ascribed to several reasons as follows. On one hand, the ability to capture CO_2 molecule for different TMIs plays an important role in photocatalytic efficiency [68,69]. Room temperature volumetric CO_2 adsorption measurements implied that TMI-modified DQTP COF possessed relatively high but different adsorption capacities (Figure S35 and Table S7) and noted that DQTP COF-Zn showed the highest CO_2 uptake ($33.13 \text{ cm}^3 \text{ g}^{-1}$). On the other hand, selective produce CO or HCOOH depends mainly on which path the catalyst tends to proceed, whereas the key factor ought to be whether the coordination environment of the metal ion is able to create a suitable condition to cleave

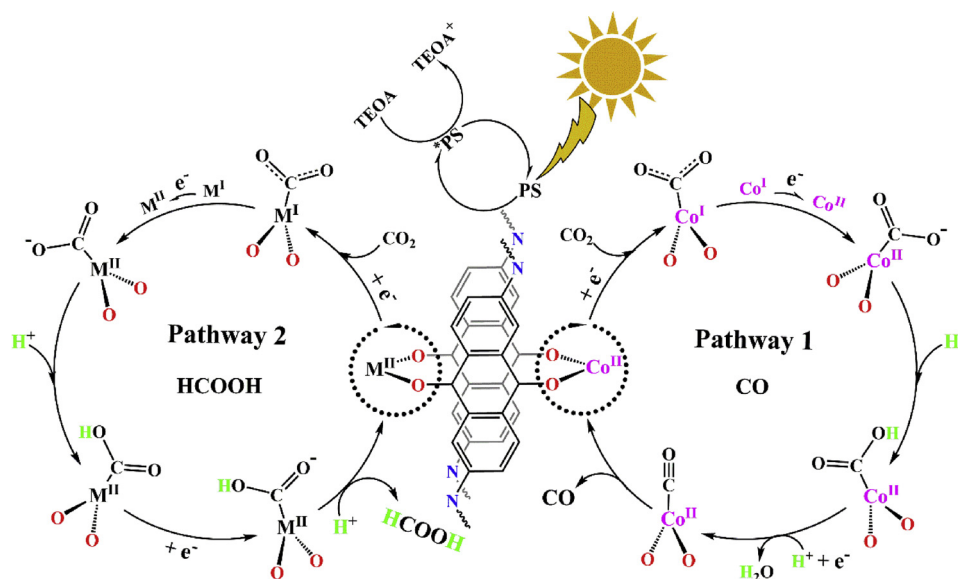


Fig. 5. Proposed mechanisms for photocatalytic reduction of CO_2 with DQTP COF-M.

C–O bond in metal– CO_2H intermediate [66]. The electron-rich coordination environment (electron donor) that can weaken and break the C–O bond tended to form CO (Fig. 5, Pathway 1), while electron-deficiency coordination environment (electron withdraw) that can enhance the C–O bonding force to a certain extent inclined to form HCOOH (Fig. 5, Pathway 2) [70]. From this point of view, Co(II) as a good π -donor usually tends to convert CO_2 to CO, while Zn(II) as a poor π -donor prones to convert CO_2 to produce HCOOH. This is precisely in line with our experimental results. For DQTP COF-Ni(II), a nearly equal amount of CO and HCOOH was produced when conducting photocatalytic CO_2 reduction reaction, indicating the probabilities of these two pathways are almost the same. Interestingly, for DQTP COF-Zn(II), only HCOOH was detected in our photocatalytic system, which means that the competitive CO evolution path may be significantly suppressed and the C–O bond in Zn–COOH intermediates is stable and unbreakable by protonation process.

4. Conclusions

In summary, we have successfully constructed a TMI-modified COF system for photocatalytic CO_2 reduction that showed high efficiency and durability for converting CO_2 to CO and/or HCOOH under visible light irradiation. The successful incorporation of TMIs into DQTP COF realized through a simple post-treatment method was verified by exhaustive characterization combined with DFT calculations. The feasibility of photoreaction was confirmed by electronic structure analysis. The core role of DQTP COF as a platform is that in the columnar orientation COFs provide a high-efficient charge carrier transport because of the ordered π -electronic pathway, which improves electron transfer from COF to metal moiety, thereby increasing the reactivity. Different kinds of open metal active species on COFs have a strong influence on the activity and selectivity of CO_2 reduction. As a result, DQTP COF-Co and Zn exhibited the highest CO and formic acid production rate of 1.02×10^3 and $152.5 \mu\text{mol h}^{-1} \text{g}^{-1}$, respectively. A “two-pathway” mechanism for photocatalytic CO_2 reduction over metal-modified COFs was proposed to explain differences in activity and selectivity. This work demonstrated the great potential of COFs as platforms for effective heterogeneous photocatalytic conversion of CO_2 , and we believe that the present strategy can open up a new avenue to the development of more efficient heterogeneous catalysts for photocatalytic CO_2 reduction.

Declarations of interest

None

Acknowledgments

This work was financially supported by NSFC [No.21622104, 21471080, 2170010097 and 21701085, BK20171032]; the NSF of Jiangsu Province of China [No. SBK2017040708]; the Natural Science Research of Jiangsu Higher Education Institutions of China [No. 17KJB150025]; Priority Academic Program Development of Jiangsu Higher Education Institutions and the Foundation of Jiangsu Collaborative Innovation Center of Biomedical Functional Materials.

Appendix A. Supplementary data

Supplementary material related to this article can be found, in the online version, at doi:<https://doi.org/10.1016/j.apcatb.2019.05.033>.

References

- [1] T.M. Wigley, The climate change commitment, *Science* 307 (2005) 1766–1769, <https://doi.org/10.1126/science.1103934>.
- [2] J. Barber, P.D. Tran, From natural to artificial photosynthesis, *J. R. Soc. Interface* 10 (2013) 20120984, <https://doi.org/10.1098/rsif.2012.0984>.
- [3] A. Cho, Energy's tricky tradeoffs, *Science* 329 (2010) 786–787, <https://doi.org/10.1126/science.329.5993.786>.
- [4] S.J. Davis, K. Caldeira, H.D. Matthews, Future CO_2 emissions and climate change from existing energy infrastructure, *Science* 329 (2010) 1330–1333, <https://doi.org/10.1126/science.1188566>.
- [5] M.D. Doherty, D.C. Grills, J.T. Muckerman, D.E. Polyansky, E. Fujita, Coord. Toward more efficient photochemical CO_2 reduction: Use of scCO_2 or photo-generated hydrides, *Chem. Rev.* 254 (2010) 2472–2482, <https://doi.org/10.1016/j.ccr.2009.12.013>.
- [6] J. Barber, Photosynthetic energy conversion: natural and artificial, *Chem. Soc. Rev.* 38 (2009) 185–196, <https://doi.org/10.1039/B802262N>.
- [7] N.S. Lewis, D.G. Nocera, Powering the planet: chemical challenges in solar energy utilization, *P. Natl. Acad. Sci.* 103 (2006) 15729–15735, <https://doi.org/10.1073/pnas.0603395103>.
- [8] V.D.B.C. Dasireddy, B. Likozar, The role of copper oxidation state in $\text{Cu/ZnO/Al}_2\text{O}_3$ catalysts in CO_2 hydrogenation and methanol productivity, *Renew. Energy* 140 (2019) 452–460, <https://doi.org/10.1016/j.renene.2019.03.073>.
- [9] M. Pori, I. Arčon, D. Lašič Jurković, M. Marinšek, G. Dražić, B. Likozar, Z. Crnjak Orel, Synthesis of a Cu/ZnO nanocomposite by electroless plating for the catalytic conversion of CO_2 to methanol, *Catal. Lett.* 149 (2019) 1427–1439, <https://doi.org/10.1007/s10562-019-02717-7>.
- [10] V.D.B.C. Dasireddy, N.S. Štefančič, M. Huš, B. Likozar, Effect of alkaline earth metal oxide (MO) $\text{Cu/MO/Al}_2\text{O}_3$ catalysts on methanol synthesis activity and selectivity via CO_2 reduction, *Fuel* 233 (2018) 103–112, <https://doi.org/10.1016/j.fuel.2018>.

- 06.046.
- [11] T.M. Suzuki, T. Takayama, S. Sato, A. Iwase, A. Kudo, T. Morikawa, Enhancement of CO₂ reduction activity under visible light irradiation over Zn-based metal sulfides by combination with Ru-complex catalysts, *Appl. Catal. B* 224 (2018) 572–578, <https://doi.org/10.1016/j.apcatb.2017.10.053>.
 - [12] J.L. White, M.F. Baruch, J.E. Pander Iii, Y. Hu, L.C. Fortmeyer, J.E. Park, T. Zhang, K. Liao, J. Gu, Y. Yan, T.W. Shaw, E. Abelev, A.B. Bocarsly, Light-Driven Heterogeneous Reduction of Carbon Dioxide: Photocatalysts and Photoelectrodes, *Chem. Rev.* 115 (2015) 12888–12935, <https://doi.org/10.1021/acs.chemrev.5b00370>.
 - [13] Z. Sun, N. Talreja, H. Tao, J. Texter, M. Muhler, J. Strunk, J. Chen, Catalysis of carbon dioxide photoreduction on nanosheets: fundamentals and challenges, *Angew. Chem. Int. Ed.* 57 (2018) 7610–7627, <https://doi.org/10.1002/anie.201710509>.
 - [14] K. Li, B. Peng, T. Peng, Recent advances in heterogeneous photocatalytic CO₂ conversion to solar fuels, *ACS Catal.* 6 (2016) 7485–7527, <https://doi.org/10.1021/acscatal.6b02089>.
 - [15] S.-L. Xie, J. Liu, L.-Z. Dong, S.-L. Li, Y.-Q. Lan, Z.-M. Su, Hetero-metallic active sites coupled with strongly reductive polyoxometalate for selective photocatalytic CO₂-to-CH₄ conversion in water, *Chem. Sci.* 10 (2019) 185–190, <https://doi.org/10.1039/C8SC03471K>.
 - [16] S. Lingampalli, M.M. Ayyub, C. Rao, Recent progress in the photocatalytic reduction of carbon dioxide, *ACS Omega* 2 (2017) 2740–2748, <https://doi.org/10.1021/acsomega.7b00721>.
 - [17] K.K. Ghuman, L.B. Hoch, P. Szymanski, J.Y. Loh, N.P. Kherani, M.A. El-Sayed, G.A. Ozin, C.V. Singh, Photoexcited surface frustrated Lewis pairs for heterogeneous photocatalytic CO₂ reduction, *J. Am. Chem. Soc.* 138 (2016) 1206–1214, <https://doi.org/10.1021/jacs.5b10179>.
 - [18] H. Takeda, O. Ishitani, Development of efficient photocatalytic systems for CO₂ reduction using mononuclear and multinuclear metal complexes based on mechanistic studies, *Coord. Chem. Rev.* 254 (2010) 346–354, <https://doi.org/10.1016/j.ccr.2009.09.030>.
 - [19] A.M. Appel, J.E. Bercaw, A.B. Bocarsly, H. Dobbek, D.L. DuBois, M. Dupuis, J.G. Ferry, E. Fujita, R. Hille, P.J. Kenis, Frontiers, opportunities, and challenges in biochemical and chemical catalysis of CO₂ fixation, *Chem. Rev.* 113 (2013) 6621–6658, <https://doi.org/10.1021/cr300463y>.
 - [20] X. Liu, S. Inagaki, J. Gong, Heterogeneous molecular systems for photocatalytic CO₂ reduction with water oxidation, *Angew. Chem. Int. Ed.* 55 (2016) 14924–14950, <https://doi.org/10.1002/anie.201600395>.
 - [21] Y. Fu, D. Sun, Y. Chen, R. Huang, Z. Ding, X. Fu, Z. Li, An amine-functionalized titanium metal-organic framework photocatalyst with visible-light-induced activity for CO₂ reduction, *Angew. Chem. Int. Ed.* 124 (2012) 3420–3423, <https://doi.org/10.1002/anie.201108357>.
 - [22] L. Shi, T. Wang, H. Zhang, K. Chang, J. Ye, Electrostatic self-assembly of nanosized carbon nitride nanosheet onto a zirconium metal-organic framework for enhanced photocatalytic CO₂ reduction, *Adv. Funct. Mater.* 25 (2015) 5360–5367, <https://doi.org/10.1002/adfm.201502253>.
 - [23] D. Wang, R. Huang, W. Liu, D. Sun, Z. Li, Fe-based MOFs for photocatalytic CO₂ reduction: role of coordination unsaturated sites and dual excitation pathways, *ACS Catal.* 4 (2014) 4254–4260, <https://doi.org/10.1021/cs501169t>.
 - [24] A.P. Cote, A.I. Benin, N.W. Ockwig, M. O'keeffe, A.J. Matzger, O.M. Yaghi, Porous, crystalline, covalent organic frameworks, *Science* 310 (2005) 1166–1170, <https://doi.org/10.1126/science.1120411>.
 - [25] N. Huang, P. Wang, D. Jiang, Covalent organic frameworks: a materials platform for structural and functional designs, *Nat. Rev. Mater.* 1 (2016) 16068, <https://doi.org/10.1038/natrevmats.2016.68>.
 - [26] C.S. Diercks, O.M. Yaghi, The atom, the molecule, and the covalent organic framework, *Science* 355 (2017), <https://doi.org/10.1126/science.aal1585>.
 - [27] Q. Fang, S. Gu, J. Zheng, Z. Zhuang, S. Qiu, Y. Yan, 3D Microporous Base-Functionalized Covalent Organic Frameworks for Size-Selective Catalysis, *Angew. Chem. Int. Ed.* 53 (2014) 2878–2882, <https://doi.org/10.1002/anie.201310500>.
 - [28] P. Su, K. Iwase, T. Harada, K. Kamiya, S. Nakanishi, Covalent triazine framework modified with coordinatively-unsaturated Co or Ni atoms for CO₂ electrochemical reduction, *Chem. Sci.* 9 (2018) 3941–3947, <https://doi.org/10.1039/C8SC00604K>.
 - [29] C.S. Diercks, S. Lin, N. Kornienko, E.A. Kapustin, E.M. Nichols, C. Zhu, Y. Zhao, C.J. Chang, O.M. Yaghi, Reticular electronic tuning of porphyrin active sites in covalent organic frameworks for electrocatalytic carbon dioxide reduction, *J. Am. Chem. Soc.* 140 (2018) 1116–1122, <https://doi.org/10.1021/jacs.7b11940>.
 - [30] X. Ding, J. Guo, X. Feng, Y. Honsho, J. Guo, S. Seki, P. Maitarad, A. Saeki, S. Nagase, D. Jiang, Synthesis of metallophthalocyanine covalent organic frameworks that exhibit high carrier mobility and photoconductivity, *Angew. Chem. Int. Ed.* 50 (2011) 1289–1293, <https://doi.org/10.1002/anie.201005919>.
 - [31] X. Wang, L. Chen, S.Y. Chong, M.A. Little, Y. Wu, W.-H. Zhu, R. Clowes, Y. Yan, M.A. Zwiijnenburg, R.S. Sprick, A.I. Cooper, Sulfone-containing covalent organic frameworks for photocatalytic hydrogen evolution from water, *Nat. Chem.* 10 (2018) 1180–1189, <https://doi.org/10.1038/s41557-018-0141-5>.
 - [32] L. Stegbauer, K. Schwinghammer, B.V. Lotsch, A hydrazone-based covalent organic framework for photocatalytic hydrogen production, *Chem. Sci.* 5 (2014) 2789–2793, <https://doi.org/10.1039/c4sc00016a>.
 - [33] J. Thote, H.B. Aiyappa, A. Deshpande, D. Diaz Diaz, S. Kurungot, R. Banerjee, A covalent organic framework-cadmium sulfide hybrid as a prototype photocatalyst for visible-light-driven hydrogen production, *Chemistry* 20 (2014) 15961–15965, <https://doi.org/10.1002/chem.201403800>.
 - [34] T. Banerjee, K. Gottschling, G. Savasci, C. Ochsenfeld, B.V. Lotsch, H₂Evolution with Covalent Organic Framework Photocatalysts, *ACS Energy Lett.* 3 (2018) 400–409, <https://doi.org/10.1021/acsenenergylett.7b01123>.
 - [35] T. Banerjee, F. Haase, G. Savasci, K. Gottschling, C. Ochsenfeld, B.V. Lotsch, Single-site photocatalytic H₂ evolution from covalent organic frameworks with molecular cobaloxime Co-catalysts, *J. Am. Chem. Soc.* 139 (2017) 16228–16234, <https://doi.org/10.1021/jacs.7b07489>.
 - [36] P. Pachfule, A. Acharjya, J. Roeser, T. Langenhahn, M. Schwarze, R. Schomacker, A. Thomas, J. Schmidt, Diacetylene functionalized covalent organic framework (COF) for photocatalytic hydrogen generation, *J. Am. Chem. Soc.* 140 (2018) 1423–1427, <https://doi.org/10.1021/jacs.7b11255>.
 - [37] L. Wang, Y. Wan, Y. Ding, S. Wu, Y. Zhang, X. Zhang, G. Zhang, Y. Xiong, X. Wu, J. Yang, H. Xu, Conjugated microporous polymer nanosheets for overall water splitting using visible light, *Adv. Mater.* 29 (2017) 1702428, <https://doi.org/10.1002/adma.201702428>.
 - [38] F.M. Zhang, J.L. Sheng, Z.D. Yang, X.J. Sun, H.L. Tang, M. Lu, H. Dong, F.C. Shen, J. Liu, Y.Q. Lan, Rational design of MOF/COF hybrid materials for photocatalytic H₂ evolution in the presence of sacrificial Electron donors, *Angew. Chem. Int. Ed.* 130 (2018) 12282–12286, <https://doi.org/10.1002/ange.201806862>.
 - [39] L. Stegbauer, S. Zech, G. Savasci, T. Banerjee, F. Podjaski, K. Schwinghammer, C. Ochsenfeld, B.V. Lotsch, Tailor-made photoconductive pyrene-based covalent organic frameworks for visible-light-Driven hydrogen generation, *Adv. Energy Mater.* 8 (2018) 1703278, <https://doi.org/10.1002/aenm.201703278>.
 - [40] R. Xu, X.-S. Wang, H. Zhao, H. Lin, Y.-B. Huang, R. Cao, Rhenium-modified porous covalent triazine framework for highly efficient photocatalytic carbon dioxide reduction in a solid-gas system, *Catal. Sci. Technol.* 8 (2018) 2224–2230, <https://doi.org/10.1039/C8CY00176F>.
 - [41] S. Yang, W. Hu, X. Zhang, P. He, B. Pattengale, C. Liu, M. Cendejas, I. Hermans, X. Zhang, J. Zhang, J. Huang, 2D covalent organic frameworks as intrinsic photocatalysts for visible light-driven CO₂ reduction, *J. Am. Chem. Soc.* 140 (2018) 14614–14618, <https://doi.org/10.1021/jacs.8b09705>.
 - [42] R.K. Yadav, A. Kumar, N.-J. Park, K.-J. Kong, J.-O. Baeg, A highly efficient covalent organic framework film photocatalyst for selective solar fuel production from CO₂, *J. Mater. Chem. A Mater. Energy Sustain.* 4 (2016) 9413–9418, <https://doi.org/10.1039/c6ta01625a>.
 - [43] S. Guo, H. Zhang, Y. Chen, Z. Liu, B. Yu, Y. Zhao, Z. Yang, B. Han, Z. Liu, Visible-Light-Driven Photoreduction of CO₂ to CH₄ over N,O,P-Containing Covalent Organic Polymer Submicrospheres, *ACS Catal.* 8 (2018) 4576–4581, <https://doi.org/10.1021/acscatal.8b00989>.
 - [44] Y. Fu, X. Zhu, L. Huang, X. Zhang, F. Zhang, W. Zhu, Azine-based covalent organic frameworks as metal-free visible light photocatalysts for CO₂ reduction with H₂O, *Appl. Catal. B* 239 (2018) 46–51, <https://doi.org/10.1016/j.apcatb.2018.08.004>.
 - [45] C.R. DeBlase, K.E. Silberstein, T.-T. Truong, H.C. Abruña, W.R. Dichtel, β-Ketoamine-linked covalent organic frameworks capable of pseudocapacitive energy storage, *J. Am. Chem. Soc.* 135 (2013) 16821–16824, <https://doi.org/10.1021/ja409421d>.
 - [46] Á. Raya-Barón, M.A. Ortuño, P. Oña-Burgos, A. Rodríguez-Diéguez, R. Langer, C.J. Cramer, I. Kuzu, I. Fernández, Efficient Hydrosilylation of Acetophenone with a New Anthraquinone Amide-Based Iron Precatalyst, *Organometallics* 35 (2016) 4083–4089, <https://doi.org/10.1021/acs.organomet.6b00765>.
 - [47] P.J. Beldon, S. Henke, B. Monserrat, S. Tominaka, N. Stock, A.K. Cheetham, Transition metal coordination complexes of chrysazin, *CrystEngComm* 18 (2016) 5121–5129, <https://doi.org/10.1039/c5ce00792e>.
 - [48] A. Mandal, A. Grupp, B. Schwederski, W. Kaim, G.K. Lahiri, Varying electronic structures of diosmium complexes from noninnocently behaving anthraquinone-derived bis-chelate ligands, *Inorg. Chem.* 54 (2015) 7936–7944, <https://doi.org/10.1021/acs.inorgchem.5b01017>.
 - [49] K. Heinze, S. Mann, G. Huttner, L. Zsolnai, Dinuclear Tripod Cobalt Complexes with Bridging 1,4,5,8-Tetraoxonaphthalene and 1,4,9,10-Tetraoxanthracene Ligands: Structures, Spectroscopic, Magnetic, and Electrochemical Properties, *Chem. Ber.* 129 (1996) 1115–1122, <https://doi.org/10.1002/cher.19961290922>.
 - [50] M.A. Khayum, S. Kandambeth, S. Mitra, S.B. Nair, A. Das, S.S. Nagane, R. Mukherjee, R. Banerjee, Chemically delaminated free-standing ultrathin covalent organic nanosheets, *Angew. Chem. Int. Ed.* 55 (2016) 15604–15608, <https://doi.org/10.1002/anie.201607812>.
 - [51] P. Bhanja, S. Mishra, K. Manna, A. Mallick, K. Das Saha, A. Bhaumik, Covalent organic framework material bearing phloroglucinol building units as a potent anticancer agent, *ACS Appl. Mater. Interfaces* 9 (2017) 31411–31423, <https://doi.org/10.1021/acsami.7b07343>.
 - [52] B.C. Patra, S. Khilari, R.N. Manna, S. Mondal, D. Pradhan, A. Pradhan, A. Bhaumik, A metal-free covalent organic polymer for electrocatalytic hydrogen evolution, *ACS Catal.* 7 (2017) 6120–6127, <https://doi.org/10.1021/acscatal.7b01067>.
 - [53] Q. Sun, B. Aguilá, J. Perman, N. Nguyen, S. Ma, Flexibility matters: cooperative active sites in covalent organic framework and threaded ionic polymer, *J. Am. Chem. Soc.* 138 (2016) 15790–15796, <https://doi.org/10.1021/jacs.6b10629>.
 - [54] H.B. Aiyappa, J. Thote, D.B. Shinde, R. Banerjee, S. Kurungot, Cobalt-modified covalent organic framework as a robust water oxidation electrocatalyst, *Chem. Mater.* 28 (2016) 4375–4379, <https://doi.org/10.1021/acs.chemmater.6b01370>.
 - [55] M.A. Khayum, V. Vijayakumar, S. Karak, S. Kandambeth, M. Bhadra, K. Suresh, N. Acharambath, S. Kurungot, R. Banerjee, Convergent covalent organic framework thin sheets as flexible supercapacitor electrodes, *ACS Appl. Mater. Interfaces* 10 (2018) 28139–28146, <https://doi.org/10.1021/acsami.8b10486>.
 - [56] S.Y. Ding, J. Gao, Q. Wang, Y. Zhang, W.G. Song, C.Y. Su, W. Wang, Construction of Covalent Organic Framework for Catalysis: Pd/COF-LZU1 in Suzuki-Miyaura Coupling Reaction, *J. Am. Chem. Soc.* 133 (2011) 19816–19822, <https://doi.org/10.1021/ja206846p>.
 - [57] Z. Nickolov, G. Georgiev, D. Stoilova, I. Ivanov, Raman and IR study of cobalt acetate dihydrate, *J. Mol. Struct.* 354 (1995) 119–125, <https://doi.org/10.1016/>

- 0022-2860(95)08877-X.
- [58] X. Chang, T. Wang, J. Gong, CO₂ photo-reduction: insights into CO₂ activation and reaction on surfaces of photocatalysts, *Energy Environ. Sci.* 9 (2016) 2177–2196, <https://doi.org/10.1039/c6ee00383d>.
- [59] Y. Tomita, S. Teruya, O. Koga, Y. Hori, Electrochemical reduction of carbon dioxide at a platinum electrode in acetonitrile-water mixtures, *J. Electrochem. Soc.* 147 (2000) 4164–4167, <https://doi.org/10.1149/1.1394035>.
- [60] Y. Pellegrin, F. Odobel, Sacrificial electron donor reagents for solar fuel production, *C. R. Chim.* 20 (2017) 283–295, <https://doi.org/10.1016/j.crci.2015.11.026>.
- [61] S. Sato, T. Morikawa, S. Saeki, T. Kajino, T. Motohiro, Visible-light-Induced selective CO₂ reduction utilizing a ruthenium complex electrocatalyst linked to a p-Type nitrogen-doped Ta₂O₅ semiconductor, *Angew. Chem. Int. Ed.* 49 (2010) 5101–5105, <https://doi.org/10.1002/anie.201000613>.
- [62] Y. Yamazaki, H. Takeda, O. Ishitani, Photocatalytic reduction of CO₂ using metal complexes, *J. Photochem. Photobiol. C Photochem. Rev.* 25 (2015) 106–137, <https://doi.org/10.1016/j.jphotochemrev.2015.09.001>.
- [63] S. Sato, T. Morikawa, T. Kajino, O. Ishitani, A highly efficient mononuclear iridium complex photocatalyst for CO₂ reduction under visible light, *Angew. Chem. Int. Ed.* 52 (2013) 988–992, <https://doi.org/10.1002/anie.201206137>.
- [64] E. Sada, H. Kumazawa, Y. Ikehara, Z.Q. Han, Chemical kinetics of the reaction of carbon dioxide with triethanolamine in non-aqueous solvents, *Chem. Eng. J.* 40 (1989) 7–12, [https://doi.org/10.1016/0300-9467\(89\)80038-3](https://doi.org/10.1016/0300-9467(89)80038-3).
- [65] G. Zhao, X. Huang, X. Wang, X. Wang, Progress in catalyst exploration for heterogeneous CO₂ reduction and utilization: a critical review, *J. Mater. Chem. A Mater. Energy Sustain.* 5 (2017) 21625–21649, <https://doi.org/10.1039/c7ta07290b>.
- [66] L. Chen, Z. Guo, X.-G. Wei, C. Gallenkamp, J. Bonin, E. Anxolabéhère-Mallart, K.-C. Lau, T.-C. Lau, M. Robert, Molecular catalysis of the electrochemical and photochemical reduction of CO₂ with earth-abundant metal complexes. Selective Production of CO vs HCOOH by Switching of the Metal Center, *J. Am. Chem. Soc.* 137 (2015) 10918–10921, <https://doi.org/10.1021/jacs.5b06535>.
- [67] A.J. Morris, G.J. Meyer, E. Fujita, Molecular approaches to the photocatalytic reduction of carbon dioxide for solar fuels, *Acc. Chem. Res.* 42 (2009) 1983–1994, <https://doi.org/10.1021/ar9001679>.
- [68] H. Zhang, J. Wei, J. Dong, G. Liu, L. Shi, P. An, G. Zhao, J. Kong, X. Wang, X. Meng, Efficient visible-light-Driven carbon dioxide reduction by a single-atom implanted metal-organic framework, *Angew. Chem. Int. Ed.* 128 (2016) 14522–14526, <https://doi.org/10.1002/anie.201608597>.
- [69] J. Kothandaraman, A. Goeppert, M. Czaun, G.A. Olah, G.S. Prakash, Conversion of CO₂ from air into methanol using a polyamine and a homogeneous ruthenium catalyst, *J. Am. Chem. Soc.* 138 (2016) 778–781, <https://doi.org/10.1021/jacs.5b12354>.
- [70] S. Chardon-Noblat, A. Deronzier, R. Ziessel, D. Zsoldos, Electroreduction of CO₂ catalyzed by polymeric [Ru(bpy)(CO)₂]_n films in aqueous media: parameters influencing the reaction selectivity, *J. Electroanal. Chem. Lausanne (Lausanne)* 444 (1998) 253–260, [https://doi.org/10.1016/S0022-0728\(97\)00584-6](https://doi.org/10.1016/S0022-0728(97)00584-6).